

Thermo-optic all-optical devices based on two-dimensional materials

KAN WU, YIFANG WANG, CIYUAN QIU,* AND JIANPING CHEN

State Key Laboratory of Advanced Optical Communication Systems and Networks, Department of Electronic Engineering, Shanghai Jiao Tong University, Shanghai 200240, China

*Corresponding author: qiciyuan@sjtu.edu.cn

Received 31 May 2018; revised 18 July 2018; accepted 19 July 2018; posted 23 July 2018 (Doc. ID 332888); published 21 August 2018

In this paper, we review our recent work on thermo-optic all-optical devices based on two-dimensional (2D) materials. The unique properties of 2D materials enable fast and highly efficient thermo-optic control of light. A few all-optical devices are demonstrated based on various thermo-optic mechanisms. Both fiber and integrated devices will be shown. © 2018 Chinese Laser Press

OCIS codes: (160.4236) Nanomaterials; (230.1150) All-optical devices; (130.3120) Integrated optics devices.

<https://doi.org/10.1364/PRJ.6.000C22>

1. INTRODUCTION

Two-dimensional (2D) materials have attracted wide attention for their unique photonic and optoelectronic properties. Since the discovery of first 2D material graphene [1–13], many 2D materials have been found, including graphene oxide [14], topological insulators (TIs) [15–18], transition metal dichalcogenides (TMDs) [19–26], black phosphorus (BP) [27–32], and MXene [33–36]. These novel 2D materials have exhibited various interesting photonic properties. For example, the controllable optical absorption by tunable Fermi level has enabled applications in compact optical modulators [4]. The wideband absorption has been utilized in photodetectors [6,29,30]. The intensity-dependent optical transmission has been widely used as saturable absorbers for ultrashort pulse generation [2,3,15,16,18,21–28,35]. The optical nonlinearity has been explored for all-optical devices, such as graphene modulators based on saturable absorption and the Kerr effect [5,10], thermo-optic switches with graphene [7,11] and phosphorene [31], and bistability devices with graphene [8]. By using graphene as a micro-heater, electrically tuned thermo-optic switches are also reported with high efficiency [12,13]. Some all-optical devices in other novel perovskite materials have also been demonstrated [37,38]. Among these demonstrations based on 2D materials, only a few thermo-optic all-optical devices have been reported, and not enough attention has been paid to this area of research.

In this paper, we summarize our recent work on all-optical devices based on 2D materials by exploring various thermo-optic mechanisms. For fiber devices, two TMD-based devices have been shown by using the wavelength-dependent absorption and thermo-optic effects of TMDs [39,40]. For integrated devices, a graphene-on-silicon nitride (Si_3N_4) switch has been

achieved by using the high thermal conductivity of graphene [41]. A comparison among current reported works of thermo-optic all-optical devices based on 2D materials is also provided.

2. FIBER DEVICES

Optical fiber provides flexibility of device fabrication and characterization. Previously, two works with graphene have been reported, and very low pump power has been achieved [7,11]. A phosphorene all-optical fiber phase modulator has also been demonstrated recently [31]. In this section, we review our work on an all-optical fiber phase shifter and switches based on 2D materials.

Different from graphene, many 2D materials exhibit wavelength-dependent absorption due to the existence of a band gap. By choosing the proper pump wavelength (control light) in a high-absorption region and signal wavelength in a low-absorption region, a thermo-optic device can be constructed [39]. Figure 1(a) shows a typical all-optical phase shifter and switch made by using tungsten disulfide (WS_2). The band gap of WS_2 near 1.3 eV (954 nm) [25] allows good absorption of the pump (control light) at 980 nm and weak absorption of the signal light near 1550 nm. The all-optical phase shifter is shown in the red frame in Fig. 1(a). It consists of two 980/1550 wavelength division multiplexers (WDMs) and a WS_2 -deposited tapered fiber. When the control light at 980 nm is applied, it is absorbed by WS_2 and generates heat. The WS_2 changes temperature and the tapered fibers change their refractive indices due to the thermo-optic effect. As a result, the 1550 nm signal light propagating through the WS_2 -deposited tapered fiber is phase-shifted accordingly.

The WS_2 nanosheets are prepared by the standard liquid-phase exfoliation (LPE) method. Briefly, bulk WS_2 powder

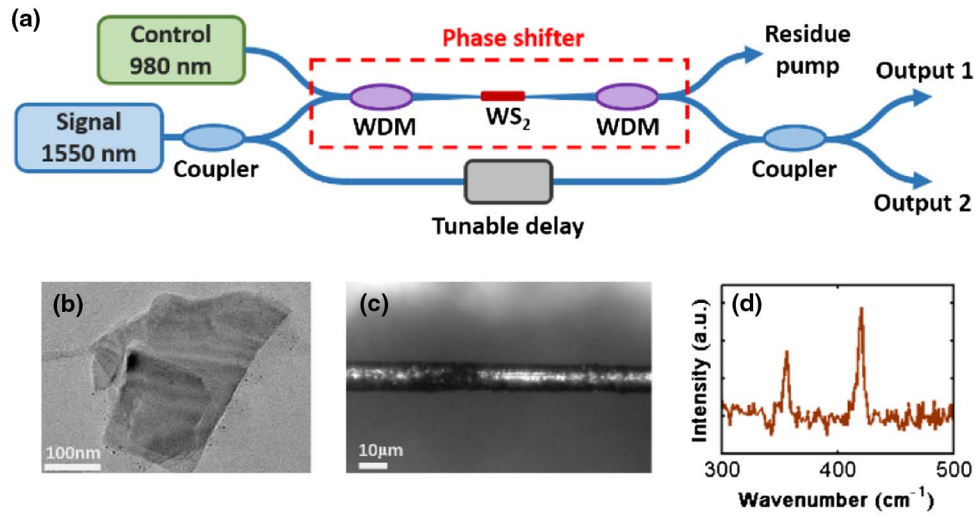


Fig. 1. (a) All-optical phase shifter and switch based on WS₂-deposited tapered fiber. (b) TEM image of WS₂ nanosheets. (c) Microscopic image of WS₂-deposited tapered fiber. (d) Raman spectrum of WS₂-deposited tapered fiber. Adapted with permission from Ref. [39].

is exfoliated into thin nanosheets by intense ultrasonic processing in a certain organic or inorganic solvent and then purified by centrifugation to remove the un-exfoliated flakes and obtain good-quality dispersions with WS₂ nanosheets. The WS₂ nanosheets' dispersions are then deposited onto a tapered fiber by using optically driven deposition. That is, when a tapered fiber is immersed in the WS₂ dispersions and proper optical power is injected to the fiber, the WS₂ nanosheets will be attracted by the optical force and attach to the tapered fiber. Figure 1(b) shows a transmission electron microscopy (TEM) image of the WS₂ nanosheets, and Fig. 1(c) shows a microscopic image of the WS₂-deposited tapered fiber. The diameter of the tapered fiber is $\sim 10 \mu\text{m}$. The length of the deposition region is $\sim 500 \mu\text{m}$. The Raman spectrum of the WS₂-deposited tapered fiber is measured, and the successful deposition of WS₂ nanosheets is confirmed, as shown in Fig. 1(d).

To measure the actual phase shift of the phase-shifter device, the device is incorporated into a fiber Mach-Zehnder interferometer (MZI). The lengths of the two arms of the MZI are unequal so that a comb-like transmission spectrum can be obtained, as shown in Fig. 2(a). When there is a phase shift induced by the control light in one arm, the spectrum would shift, and the corresponding phase shift can be calculated based on this spectral shift. Figure 2(a) shows two spectra at 0 phase shift without control light (blue) and 5π phase shift with control light (red). Figure 2(b) shows the relation between the phase shift and the control light power. The slope efficiency is $\sim 0.0174\pi \text{ mW}^{-1}$. Normalizing to the length of the interaction region (i.e., $500 \mu\text{m}$), a control efficiency of $0.035\pi \text{ mW}^{-1} \cdot \text{mm}^{-1}$ is obtained. The phase shifter has an insertion loss of 3.5 dB at 1550 nm and 5 dB at 980 nm. This insertion loss is affected by the scattering loss of the randomly deposited WS₂ materials. Using chemical vapor deposition (CVD)-grown WS₂ thin film can help to reduce the scattering loss.

It is well known that an MZI converts the phase difference to the power variation and the two output ports of the MZI have complementary output. Therefore, the MZI with

WS₂-deposited tapered fiber in one arm can function as an all-optical switch. An experimental result is shown in Fig. 2(c). The control light is a square wave (yellow), and the 1550 nm output signal at the output 1 port is a bright pulse train (blue). The complementary output signal at the output 2 port is a dark pulse train shown in Fig. 2(d). An exponential fit of the bright pulse in Fig. 2(c) indicates that the switch has a rise time constant of 7.3 ms and a fall time constant of 3.5 ms.

The thermo-optic coefficient of WS₂ can be estimated. By simulation, the optical power percentage is $\sim 96\%$ in the tapered fiber and $\sim 3\%$ in WS₂ both for 980 and 1550 nm. By increasing the pump power until the WS₂ material reaches its decomposition temperature in the air (with other samples),

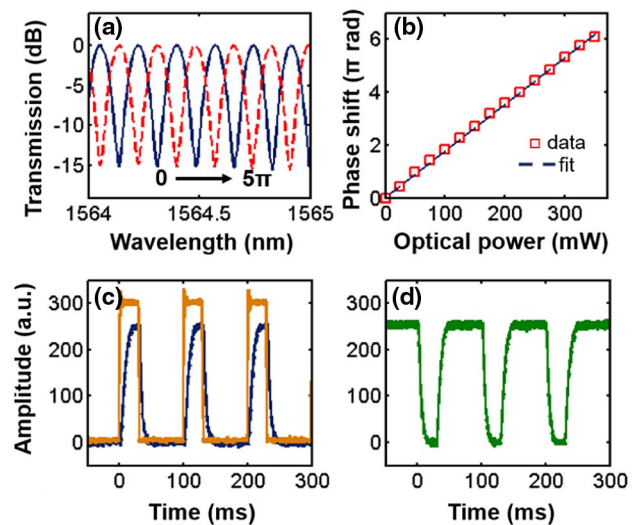


Fig. 2. (a) Transmission spectra of the MZI with 0 (blue) and 5π phase shift (red). (b) Relation between the phase shift and the control light power. (c) Pulsed control light (yellow) and switch output at output 1 port (blue). (d) Complementary output at output 2 port. Adapted with permission from Ref. [39].

we roughly estimate that the local temperature change of WS₂ tapered fiber is 40–60 K for a π phase shift. The corresponding index change is $\Delta n = 1.08 \times 10^{-3}$ for an interaction length of 500 μm . The contribution of index change can be roughly estimated by $\Delta n = \Delta n_{\text{WS}_2} \cdot 3\% + \Delta n_{\text{TF}} \cdot 96\%$ (see Appendix A). Noting that the thermo-optic coefficient for silica fiber is $\sim 1.1 \times 10^{-5}/\text{K}$, and the index change of tapered fiber Δn_{TF} is $(4.4 - 6.6) \times 10^{-4}$ for a temperature change of 40–60 K. The index change of WS₂ Δn_{WS_2} is then found to be $(1.49 - 2.19) \times 10^{-2}$, corresponding to a thermo-optic coefficient of $(2.48 - 5.48) \times 10^{-4}/\text{K}$. To further confirm the estimation of the thermo-optic coefficient of WS₂, an ellipsometric measurement has been performed. The WS₂ sample is prepared by the CVD method on a sapphire substrate, and the sample is grown to a very large thickness of ~ 200 nm to meet the requirement of the ellipsometer. Figure 3(a) shows the refractive index calculated from the measurement data, and Fig. 3(b) is the index change at different temperatures. A thermo-optic coefficient of $3.36 \times 10^{-4}/\text{K}$ is obtained. Although WS₂ with

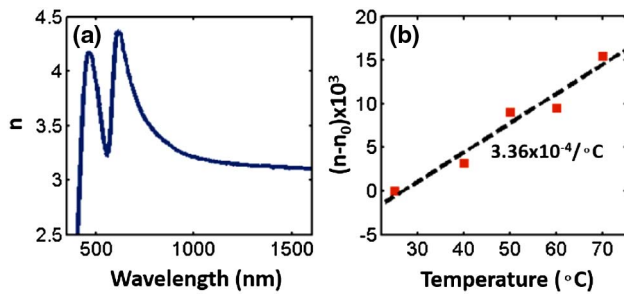


Fig. 3. (a) Refractive index of WS₂ from ellipsometric measurement and (b) refractive index change at different temperatures. Adapted with permission from Ref. [39].

different thicknesses may have different thermo-optic properties, the analyses based on power distribution and based on ellipsometric measurement both indicate a coefficient of $\sim 10^{-4}/\text{K}$, which is believed to represent the actual thermo-optic property of WS₂. This result indicates that WS₂ and tapered fiber have nearly equal contributions to the index change.

The device performance can be further improved by applying a new design [40], as shown in Fig. 4(a). The MZI structure in Fig. 1(a) is sensitive to environmental perturbation because the perturbations on the two arms are usually different and can affect the output. Another problem is that the deposition region is still long, which makes the response speed of the device low. To improve this, Fig. 4(a) shows a new all-optical switch with a polarization interferometer and a TMD-polymer thin film. Here, a MoS₂-polyvinyl alcohol (PVA) thin film is fabricated. MoS₂ nanosheet dispersions are prepared by the LPE method described above. Then the dispersions are mixed with a PVA solution and dried on a clean plastic dish under 50 $^{\circ}\text{C}$ for 3 days to form the thin film. Figure 4(b) shows the fabricated MoS₂-PVA thin film and the film when it is cut and transferred to a fiber end.

The device principle can be explained by Fig. 4(c). The x - y plane is perpendicular to the direction of light propagation. By adjusting the polarization controllers (PCs), the polarization of the signal light is set to the E_1 direction with equal projection E_x and E_y on the x and y axes. The direction of the polarizer is perpendicular to E_1 so that the original polarizer output is very low. When the control light at 980 nm is applied, the MoS₂-PVA thin film absorbs the light power and generates heat. However, due to the naturally non-uniform distribution of the MoS₂ nanosheets in the PVA film, the heat distribution is not uniform either. This non-uniform heat distribution leads to a non-uniform index change and thus unequal phase shift to E_x and E_y . In Fig. 4(c), the relative phase of E_x is shifted by π ,

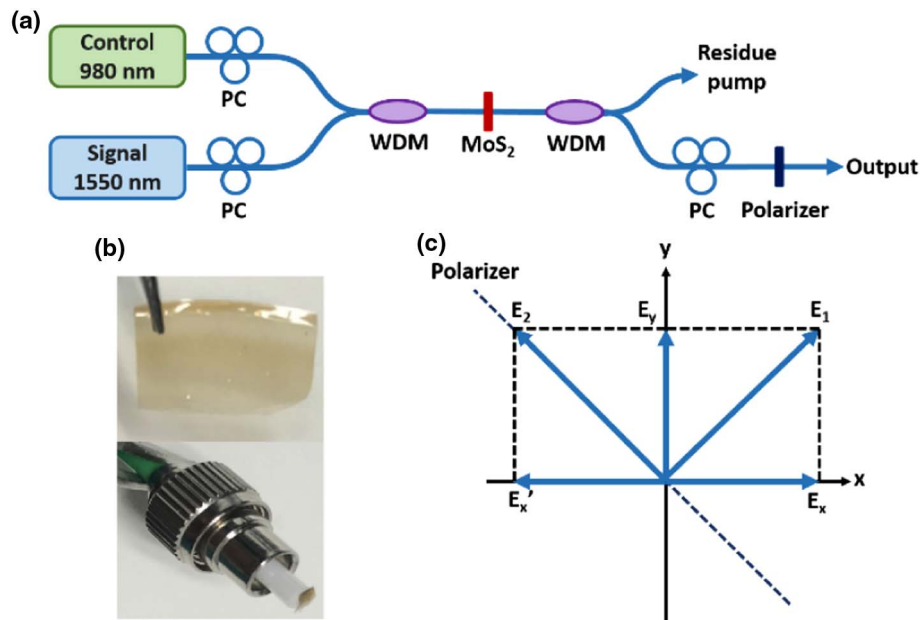


Fig. 4. (a) All-optical switch based on polarization interferometer and MoS₂-PVA thin film. (b) MoS₂-PVA thin film. (c) Device principle. Adapted with permission from Ref. [40].

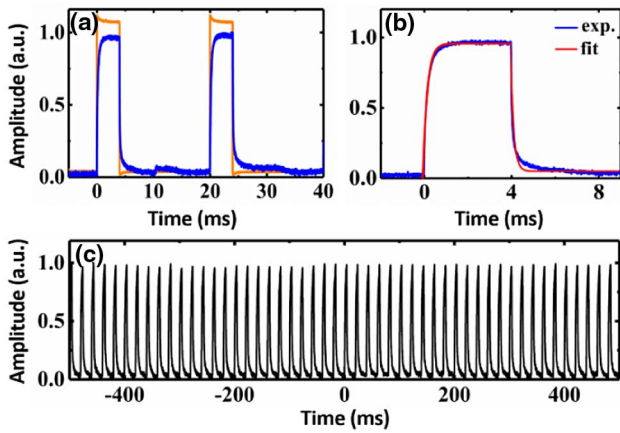


Fig. 5. (a) Pulsed control light (yellow) and output signal (blue). (b) A zoomed view of a single off-on-off transition of the output pulse (blue) and exponential fit (red). (c) A long-term stable output pulse train. Adapted with permission from Ref. [40].

and E_x becomes E'_x with the control light applied. The new polarization direction of the signal then becomes E_2 , which has high transmission in the polarizer.

Figure 5(a) shows the output signal pulses (blue) from the polarizer when square-wave control pulses are applied (yellow). Figure 5(b) is a zoomed view of a single output pulse. By exponential fitting, the pulse has a rise time constant of 324.5 μ s and a fall time constant of 286.7 μ s. Compared with the WS_2 -deposited tapered fiber in the MZI design, the MoS_2 -PVA thin film allows much faster heat distribution and thus results in a more than 10 times faster switching time. Moreover, two interference beams share the same fiber in the polarization interferometer, and the output pulses are less sensitive to the environmental perturbation. Figure 5(c) shows a long-term output pulse train, and very stable output can be observed.

It should also be noted that the contribution of the saturable absorption of the TMD materials is negligible in

the experiment because the modulation depth of TMD materials is only a few percent (the on-off power ratio is 10–15 dB in our work), and the saturation intensity is relatively high (20 MW/cm^2 intensity means 16 W power in fiber).

3. INTEGRATED DEVICE

To further improve the response time and shrink the footprint of the device, a graphene-on-silicon nitride (Si_3N_4) all-optical switch is proposed and demonstrated [41]. Previously, a similar device has been reported for thermo-optic bistability [8], and graphene has also been used as an efficient thermal heater in silicon devices [12,13]. In this work, the high thermal conductivity of graphene is utilized to efficiently transfer the heat to the waveguide and improve the switching speed.

Figures 6(a) and 6(b) show the experimental setup and the schematic diagram of the switch, which consists of a Si_3N_4 micro-ring resonator (MRR) with a graphene sheet on top. The diameter for the MRR is 60 μm . A straight waveguide is side-coupled to the MRR with a gap distance set to 100 nm. The dimensions for the straight waveguide and the waveguide forming the MRR are 1.2 $\mu\text{m} \times 400$ nm. To enhance the coupling between the waveguides and tapered lensed fibers, inverse tapers are integrated at the input and output terminals of the waveguides.

The device fabrication starts on a commercial wafer with a 400-nm-thick top Si_3N_4 layer and a 5- μm -thick buried oxide layer. Standard electron beam lithography (EBL) and inductive coupling plasma (ICP) etching processes are used to define the device structure. Then CVD-grown graphene on a copper foil is wet-transferred on top of it. The graphene layer is then patterned by EBL and an oxygen plasma etching process. As shown in the scanning electron microscope (SEM) image of the device in Fig. 6(c), only part of the MRR is covered by the graphene sheet, whose length is ~ 43.4 μm . Thus, the loss from the graphene layer can be reduced.

Figure 6(d) shows the principle of the thermo-optic tuning switch. The solid line is the initial transmission spectrum.

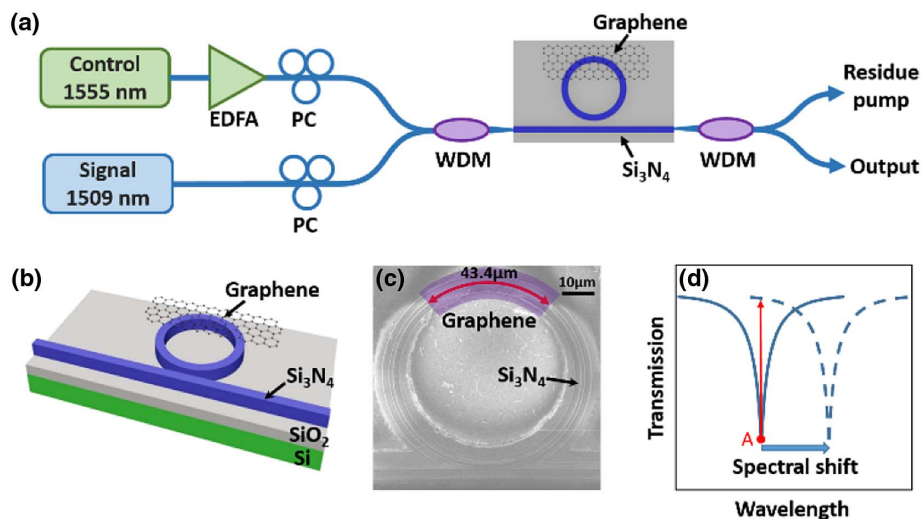


Fig. 6. (a) All-optical switch based on a graphene-on- Si_3N_4 device. (b) Device structure. (c) SEM image of device. (d) Device principle. Adapted with permission from Ref. [41].

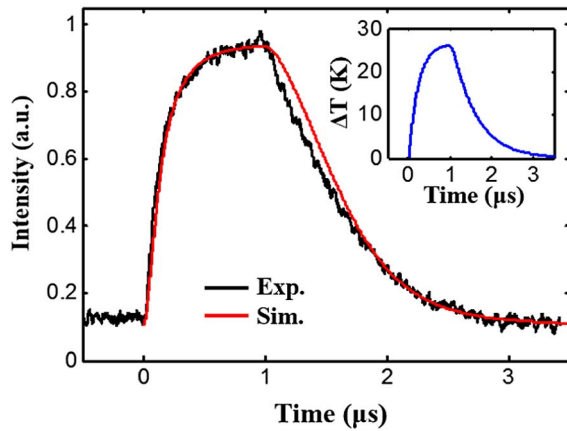


Fig. 7. Experimental (black) and simulation (red) results of an output signal pulse. Inset: temperature change of the device. Adapted with permission from Ref. [41].

When the optical control light at 1555 nm is injected into the device, part of the optical power is absorbed by the graphene layer and converted into heat. Then the heat can be directly transferred to the Si_3N_4 waveguide under the graphene. Thus, the transmission spectrum is red-shifted to the dash line due to the thermo-optic effect of Si_3N_4 . Denoted as point A in Fig. 6(d), the transmission of the signal light at 1509 nm will be changed accordingly if its wavelength is set near the resonance wavelength.

The experimental setup is shown in Fig. 6(a). The control light at 1555 nm is first injected into an erbium-doped fiber amplifier (EDFA) for amplification. The wavelength of the control light matches the resonance wavelength of the MRR to maximize the power absorption. The signal light at 1509 nm matches another resonance wavelength to minimize the output power, as described in Fig. 6(d). The control and signal light beams are combined through a WDM and coupled to the chip through a lensed fiber. Here, both the control light and signal light are controlled by the polarization controllers to be quasi-transverse-electric (TE) polarized. The output light is coupled out by a second lensed fiber, and a WDM follows to separate the control light and the signal light. The signal light is then characterized by an oscilloscope to observe the all-optical switching process.

Figure 7 shows the dynamic switching property of the device when a pulsed control light is applied. The control light has a repetition rate of 200 kHz, a pulse width of 1 μs , an injected

average power of 40 mW, and a peak power of 200 mW. By exponential fitting, the output signal pulse has a rise time constant of 253.0 ns and a fall time constant of 888.3 ns. The switching time is much faster than that of the conventional integrated thermo-optical switch [typically a few microseconds (μs)] due to ultra-high thermal conductivity of graphene. To further understand the physical mechanism of the device, a simulation based on coupled-mode theory (CMT) has been performed. The simulation result is shown in red in Fig. 7. It can be seen that the experimental result can be well reproduced by the simulation. The temperature change of the device is also shown in the inset of Fig. 7. The maximum temperature change and wavelength shift are calculated to be ~ 26 K and ~ 0.45 nm, respectively. The corresponding slope is 0.0173 nm/K, which is comparable to the reported experimental results in Refs. [42,43]. More details of the CMT-based simulation can be found in Ref. [41].

It is worth mentioning that we have tried all three of our fiber and integrated devices with a fast pump pulse train of 10 GHz, and no modulation has been observed on the output probe signal. All the probe signal outputs show a rise time of the millisecond level for fiber systems and microsecond level for an integrated system, which are consistent with those of previously reported thermo-optic devices. This result indicates that the thermo-optic effect is the dominant mechanism in our devices rather than other fast nonlinear processes, such as the Kerr effect.

4. DISCUSSION

To summarize the progress of thermo-optic all-optical devices based on 2D materials, a comparison between our works and other reported works is provided in Table 1. In the table, a parameter called control efficiency is defined as the phase shift [with the unit of π radians (rad)] normalized to the pump power [with the unit of milliwatts (mW)] and the light-material interaction length [with the unit of millimeters (mm)].

For the fiber-based devices, three works use fiber MZIs with different 2D materials. The work with an MZI and graphene shows a very low pump power of 5.2 mW for π phase shift due to the long interaction length of CVD graphene [7]. Our work with an MZI and WS_2 has a low insertion loss of 3.5 dB at a signal wavelength of 1550 nm, benefitting from the low absorption of WS_2 at long wavelengths while maintaining a relatively good control efficiency of $0.035\pi \text{ mW}^{-1} \cdot \text{mm}^{-1}$ [39]. The work with an MZI and fluorinated phosphorene utilizes the good pump absorption of phosphorene and obtains a

Table 1. Comparison of Reported Works of Thermo-Optic All-Optical Switches Based on 2D Materials

Device	Integration	Switching Time Const.	Extinction Ratio	Control Efficiency	Reference
Fiber MZI w/graphene	No	3.2 ms	20 dB	$0.018\pi \text{ mW}^{-1} \cdot \text{mm}^{-1}$	[7]
Fiber MZI w/ WS_2	No	7.3 ms	15 dB	$0.035\pi \text{ mW}^{-1} \cdot \text{mm}^{-1}$	Our work [39]
Fiber MZI w/phosphorene	No	2.5 ms	17 dB	NA ^a	[31]
Fiber PI w/ MoS_2	No	324.5 μs	10 dB	$0.063\pi \text{ mW}^{-1} \cdot \text{mm}^{-1}$	Our work [40]
Fiber micro-ring w/graphene	No	$\sim 134 \mu\text{s}^b$	13 dB	$0.31\pi \text{ mW}^{-1} \cdot \text{mm}^{-1}$	[11]
Si_3N_4 micro-ring w/graphene	Yes	253 ns	10 dB	$0.065\pi \text{ mW}^{-1} \cdot \text{mm}^{-1}$	Our work [41]

^aThe deposition length of the phosphorene material was not mentioned in Ref. [31].

^bEstimated from Fig. 5(b) in Ref. [11].

relatively fast rise time constant of 2.5 ms and low pump power of 34.5 mW [31]. For our work with a polarization interferometer and MoS₂, the device exhibits a fast rise time constant of 324.5 μ s due to the short interaction length [40]. For the work with a fiber micro-ring resonator and graphene, the small footprint and ring enhancement allow an even faster rise time constant of \sim 134 μ s and a very high control efficiency of 0.31 π /mW/mm [11].

For the integrated devices, to the best of our knowledge, our graphene-on-Si₃N₄ device seems to be the only reported thermo-optic all-optical switch based on 2D materials. The device has a very fast rise time constant of 253 ns and a good control efficiency of 0.065 π mW⁻¹ · mm⁻¹ enabled by the small footprint and high thermal conductivity of graphene [41].

5. CONCLUSIONS

In conclusion, we review our recent works on all-optical devices based on 2D materials by exploring various thermo-optic mechanisms. The unique properties of 2D materials allow fast and highly efficient all-optical control of light. A comparison among current reported works on thermo-optic all-optical devices based on 2D materials is also provided. The compactness of 2D materials makes them ideal candidates as light interaction media for both fiber and integrated platforms.

APPENDIX A

In the appendix, we briefly explain the equation $\Delta n = \Delta n_{\text{WS}_2} \cdot 3\% + \Delta n_{\text{TE}} \cdot 96\%$ for the estimation of index change. This equation is based on some empirical relations on conventional fiber. Here we use a standard single-mode fiber to explain this equation. We do not use the WS₂-deposited tapered fiber in the following simulation because the dimensional difference is too large between WS₂ and fiber, and the simulation result is less accurate. Figure 8(a) is the mode distribution (power) of a standard single-mode fiber by 2D simulation, and the power percentage in the core area is \sim 70%. The core index is 1.44, and the cladding index is 1.434816. The calculated effective index is 1.4370. Figure 8(b) is the change of the effective index with the change of the core index by simulation. The straight line has a slope of 0.7. Figure 8(c) is the change of the effective index with the change of the cladding index. The straight line has a slope of 0.3. Therefore, the relation of $\Delta n = \Delta n_{\text{core}} \cdot 70\% + \Delta n_{\text{clad}} \cdot 30\%$ can be used to estimate

the contribution to index change in a standard single-mode fiber. Similarly, we use $\Delta n = \Delta n_{\text{WS}_2} \cdot 3\% + \Delta n_{\text{TF}} \cdot 96\%$ to estimate the index change induced by WS₂ and a tapered fiber.

Funding. National Natural Science Foundation of China (NSFC) (61505104, 61505105, 61535006); Open Fund of IPOC (BUPT).

REFERENCES

1. F. Bonaccorso, Z. Sun, T. Hasan, and A. C. Ferrari, "Graphene photonics and optoelectronics," *Nat. Photonics* **4**, 611–622 (2010).
2. Z. Q. Luo, M. Zhou, J. Weng, G. M. Huang, H. Y. Xu, C. C. Ye, and Z. P. Cai, "Graphene-based passively Q-switched dual-wavelength erbium-doped fiber laser," *Opt. Lett.* **35**, 3709–3711 (2010).
3. Z. P. Sun, T. Hasan, F. Torrisi, D. Popa, G. Privitera, F. Q. Wang, F. Bonaccorso, D. M. Basko, and A. C. Ferrari, "Graphene mode-locked ultrafast laser," *ACS Nano* **4**, 803–810 (2010).
4. M. Liu, X. B. Yin, E. Ulin-Avila, B. S. Geng, T. Zentgraf, L. Ju, F. Wang, and X. Zhang, "A graphene-based broadband optical modulator," *Nature* **474**, 64–67 (2011).
5. W. Li, B. G. Chen, C. Meng, W. Fang, Y. Xiao, X. Y. Li, Z. F. Hu, Y. X. Xu, L. M. Tong, H. Q. Wang, W. T. Liu, J. M. Bao, and Y. R. Shen, "Ultrafast all-optical graphene modulator," *Nano Lett.* **14**, 955–959 (2014).
6. F. N. Xia, T. Mueller, Y. M. Lin, A. Valdes-Garcia, and P. Avouris, "Ultrafast graphene photodetector," *Nat. Nanotechnol.* **4**, 839–843 (2009).
7. X. T. Gan, C. Y. Zhao, Y. D. Wang, D. Mao, L. Fang, L. Han, and J. L. Zhao, "Graphene-assisted all-fiber phase shifter and switching," *Optica* **2**, 468–471 (2015).
8. Y. Gao, W. Zhou, X. Sun, H. K. Tsang, and C. Shu, "Cavity-enhanced thermo-optic bistability and hysteresis in a graphene-on-Si₃N₄ ring resonator," *Opt. Lett.* **42**, 1950–1953 (2017).
9. K.-J. Peng, C.-L. Wu, Y.-H. Lin, H.-Y. Wang, C.-H. Cheng, Y.-C. Chi, and G.-R. Lin, "Saturated evanescent-wave absorption of few-layer graphene-covered side-polished single-mode fiber for all-optical switching," *Nanophotonics* **7**, 207–215 (2018).
10. S. Yu, X. Wu, K. Chen, B. Chen, X. Guo, D. Dai, L. Tong, W. Liu, and Y. R. Shen, "All-optical graphene modulator based on optical Kerr phase shift," *Optica* **3**, 541–544 (2016).
11. Y. Wang, X. Gan, C. Zhao, L. Fang, D. Mao, Y. Xu, F. Zhang, T. Xi, L. Ren, and J. Zhao, "All-optical control of microfiber resonator by graphene's photothermal effect," *Appl. Phys. Lett.* **108**, 171905 (2016).
12. S. Yan, X. Zhu, L. H. Frandsen, S. Xiao, N. A. Mortensen, J. Dong, and Y. Ding, "Slow-light-enhanced energy efficiency for graphene micro-heaters on silicon photonic crystal waveguides," *Nat. Commun.* **8**, 14411 (2017).
13. L. Yu, Y. Yin, Y. Shi, D. Dai, and S. He, "Thermally tunable silicon photonic microdisk resonator with transparent graphene nanoheaters," *Optica* **3**, 159–166 (2016).

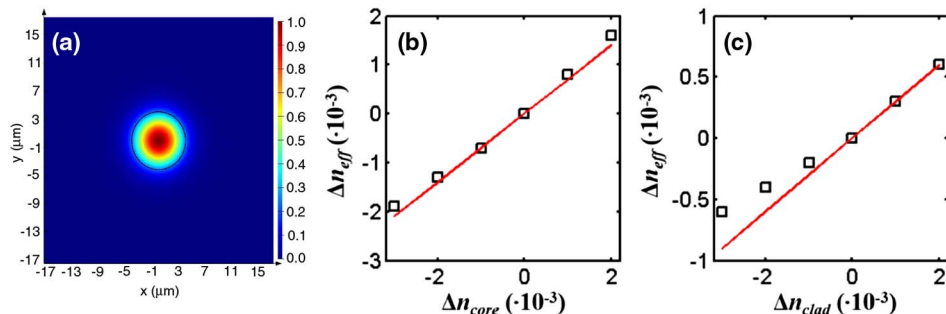


Fig. 8. (a) Mode distribution in a single-mode fiber. Relation between (b) index change and core index change, and (c) index change and cladding index change.

14. D. A. Dikin, S. Stankovich, E. J. Zimney, R. D. Piner, G. H. B. Dommett, G. Evmenenko, S. T. Nguyen, and R. S. Ruoff, "Preparation and characterization of graphene oxide paper," *Nature* **448**, 457–460 (2007).
15. Z. C. Luo, M. Liu, H. Liu, X. W. Zheng, A. P. Luo, C. J. Zhao, H. Zhang, S. C. Wen, and W. C. Xu, "2 GHz passively harmonic mode-locked fiber laser by a microfiber-based topological insulator saturable absorber," *Opt. Lett.* **38**, 5212–5215 (2013).
16. P. G. Yan, R. Y. Lin, S. C. Ruan, A. J. Liu, H. Chen, Y. Q. Zheng, S. F. Chen, C. Y. Guo, and J. G. Hu, "A practical topological insulator saturable absorber for mode-locked fiber laser," *Sci. Rep.* **5**, 8690 (2015).
17. Y.-H. Lin, C.-Y. Yang, S.-F. Lin, W.-H. Tseng, Q. Bao, C.-I. Wu, and G.-R. Lin, "Soliton compression of the erbium-doped fiber laser weakly started mode-locking by nanoscale p-type Bi_2Te_3 topological insulator particles," *Laser Phys. Lett.* **11**, 055107 (2014).
18. Y.-H. Lin, S.-F. Lin, Y.-C. Chi, C.-L. Wu, C.-H. Cheng, W.-H. Tseng, J.-H. He, C.-I. Wu, C.-K. Lee, and G.-R. Lin, "Using n- and p-type Bi_2Te_3 topological insulator nanoparticles to enable controlled femtosecond mode-locking of fiber lasers," *ACS Photon.* **2**, 481–490 (2015).
19. Q. H. Wang, K. Kalantar-Zadeh, A. Kis, J. N. Coleman, and M. S. Strano, "Electronics and optoelectronics of two-dimensional transition metal dichalcogenides," *Nat. Nanotechnol.* **7**, 699–712 (2012).
20. K. P. Wang, J. Wang, J. T. Fan, M. Lotya, A. O'Neill, D. Fox, Y. Y. Feng, X. Y. Zhang, B. X. Jiang, Q. Z. Zhao, H. Z. Zhang, J. N. Coleman, L. Zhang, and W. J. Blau, "Ultrafast saturable absorption of two-dimensional MoS_2 nanosheets," *ACS Nano* **7**, 9260–9267 (2013).
21. W. J. Liu, L. H. Pang, H. N. Han, K. Bi, M. Lei, and Z. Y. Wei, "Tungsten disulphide for ultrashort pulse generation in all-fiber lasers," *Nanoscale* **9**, 5806–5811 (2017).
22. K. Wu, X. Y. Zhang, J. Wang, X. Li, and J. P. Chen, " WS_2 as a saturable absorber for ultrafast photonic applications of mode-locked and Q-switched lasers," *Opt. Express* **23**, 11453–11461 (2015).
23. D. Mao, Y. D. Wang, C. J. Ma, L. Han, B. Q. Jiang, X. T. Gan, S. J. Hua, W. D. Zhang, T. Mei, and J. L. Zhao, " WS_2 mode-locked ultrafast fiber laser," *Sci. Rep.* **5**, 7965 (2015).
24. M. Zhang, R. C. T. Howe, R. I. Woodward, E. J. R. Kelleher, F. Torrisi, G. H. Hu, S. V. Popov, J. R. Taylor, and T. Hasan, "Solution processed MoS_2 -PVA composite for sub-bandgap mode-locking of a wideband tunable ultrafast Er:fiber laser," *Nano Res.* **8**, 1522–1534 (2015).
25. B. H. Chen, X. Y. Zhang, K. Wu, H. Wang, J. Wang, and J. P. Chen, "Q-switched fiber laser based on transition metal dichalcogenides MoS_2 , MoSe_2 , WS_2 , and WSe_2 ," *Opt. Express* **23**, 26723–26737 (2015).
26. R. I. Woodward, E. J. R. Kelleher, R. C. T. Howe, G. Hu, F. Torrisi, T. Hasan, S. V. Popov, and J. R. Taylor, "Tunable Q-switched fiber laser based on saturable edge-state absorption in few-layer molybdenum disulfide (MoS_2)," *Opt. Express* **22**, 31113–31122 (2014).
27. Z. C. Luo, M. Liu, Z. N. Guo, X. F. Jiang, A. P. Luo, C. J. Zhao, X. F. Yu, W. C. Xu, and H. Zhang, "Microfiber-based few-layer black phosphorus saturable absorber for ultra-fast fiber laser," *Opt. Express* **23**, 20030–20039 (2015).
28. J. Sotor, G. Sobon, W. Macherzynski, P. Paletko, and K. M. Abramski, "Black phosphorus saturable absorber for ultrashort pulse generation," *Appl. Phys. Lett.* **107**, 051108 (2015).
29. N. Youngblood, C. Chen, S. J. Koester, and M. Li, "Waveguide-integrated black phosphorus photodetector with high responsivity and low dark current," *Nat. Photonics* **9**, 247–252 (2015).
30. M. Q. Huang, M. L. Wang, C. Chen, Z. W. Ma, X. F. Li, J. B. Han, and Y. Q. Wu, "Broadband black-phosphorus photodetectors with high responsivity," *Adv. Mater.* **28**, 3481–3485 (2016).
31. Y. Wang, F. Zhang, X. Tang, X. Chen, Y. Chen, W. Huang, Z. Liang, L. Wu, Y. Ge, Y. Song, J. Liu, D. Zhang, J. Li, and H. Zhang, "All-optical phosphorene phase modulator with enhanced stability under ambient conditions," *Laser Photon. Rev.* **12**, 1800016 (2018).
32. J. Zheng, Z. Yang, C. Si, Z. Liang, X. Chen, R. Cao, Z. Guo, K. Wang, Y. Zhang, J. Ji, M. Zhang, D. Fan, and H. Zhang, "Black phosphorus based all-optical-signal-processing: toward high performances and enhanced stability," *ACS Photon.* **4**, 1466–1476 (2017).
33. M. Naguib, J. Come, B. Dyatkin, V. Presser, P.-L. Taberna, P. Simon, M. W. Barsoum, and Y. Gogotsi, "MXene: a promising transition metal carbide anode for lithium-ion batteries," *Electrochem. Commun.* **16**, 61–64 (2012).
34. X. Wang, S. Kajiyama, H. Iinuma, E. Hosono, S. Oro, I. Moriguchi, M. Okubo, and A. Yamada, "Pseudocapacitance of MXene nanosheets for high-power sodium-ion hybrid capacitors," *Nat. Commun.* **6**, 6544 (2015).
35. Y. I. Jhon, J. Koo, B. Anasori, M. Seo, J. H. Lee, Y. Gogotsi, and Y. M. Jhon, "Metallic MXene saturable absorber for femtosecond mode-locked lasers," *Adv. Mater.* **29**, 1702496 (2017).
36. X. T. Jiang, S. X. Liu, W. Y. Liang, S. J. Luo, Z. L. He, Y. Q. Ge, H. D. Wang, R. Cao, F. Zhang, Q. Wen, J. Q. Li, Q. L. Bao, D. Y. Fan, and H. Zhang, "Broadband nonlinear photonics in few-layer MXene $\text{Ti}_3\text{C}_2\text{T}_x$ ($T = \text{F}, \text{O}, \text{or OH}$)," *Laser Photon. Rev.* **12**, 1870013 (2018).
37. T.-C. Wei, S. Mookapati, T.-Y. Li, C.-H. Lin, G.-R. Lin, C. Jagadish, and J.-H. He, "Nonlinear absorption applications of $\text{CH}_3\text{NH}_3\text{PbBr}_3$ perovskite crystals," *Adv. Funct. Mater.* **28**, 1707175 (2018).
38. T.-C. Wei, H.-P. Wang, H.-J. Liu, D.-S. Tsai, J.-J. Ke, C.-L. Wu, Y.-P. Yin, Q. Zhan, G.-R. Lin, Y.-H. Chu, and J.-H. He, "Photostriction of strontium ruthenate," *Nat. Commun.* **8**, 15018 (2017).
39. K. Wu, C. S. Guo, H. Wang, X. Y. Zhang, J. Wang, and J. P. Chen, "All-optical phase shifter and switch near 1550 nm using tungsten disulfide (WS_2) deposited tapered fiber," *Opt. Express* **25**, 17639–17649 (2017).
40. Y. F. Wang, K. Wu, and J. P. Chen, "All-optical modulator based on MoS_2 -PVA thin film," *Chin. Opt. Lett.* **16**, 020003 (2018).
41. C. Y. Qiu, Y. X. Yang, C. Li, Y. F. Wang, K. Wu, and J. P. Chen, "All-optical control of light on a graphene-on-silicon nitride chip using thermo-optic effect," *Sci. Rep.* **7**, 7 (2017).
42. G.-R. Lin, S.-P. Su, C.-L. Wu, Y.-H. Lin, B.-J. Huang, H.-Y. Wang, C.-T. Tsai, C.-I. Wu, and Y.-C. Chi, "Si-rich SiN_x based Kerr switch enables optical data conversion up to 12 Gbit/s," *Sci. Rep.* **5**, 9611 (2015).
43. S.-P. Su, C.-L. Wu, C.-H. Cheng, B.-J. Huang, H.-Y. Wang, C.-T. Tsai, Y.-H. Lin, Y.-C. Chi, M.-H. Shih, C.-K. Lee, and G.-R. Lin, "Nonstoichiometric SiC bus/ring waveguide based all-optical data format follower and inverter," *ACS Photon.* **3**, 806–818 (2016).